

Article

Role of aluminium doping in tailoring the structural, electrical, and magnetic characteristics of Li-Co ferrites using sol-gel auto-combustion synthesis

Khushal P. Mudholkar¹, Madhu G. Kottad¹, Shivanand V. Angadi¹, Lingaraj D. Horakeri¹, Sushant S. Kakati², Shridhar N. Mathad^{2*}, Chidanandayya S. Hiremath³, Rangappa B. Pujar¹, Mahesh S. Bannur⁴

¹ Department of Physics, P. C. Jabin Science College, Hubballi 580021, India

² Department of Engineering Physics, K. L. E. Institute of Technology, Hubballi 580027, India

³ Department of Physics, S. K. Arts and H. S. Kotambari Science Institute, Hubballi 580021, India

⁴ Department of Physics, A. G. M. Rural College of Engineering and Technology, Varur, Hubballi 581207, India

* Corresponding author: Shridhar N. Mathad, physicssiddu@gmail.com, physicssiddu@kleit.ac.in

CITATION

Mudholkar KP, Kottad MG, Angadi SV, et al. Role of aluminium doping in tailoring the structural, electrical, and magnetic characteristics of Li-Co ferrites using sol-gel auto-combustion synthesis. *Characterization and Application of Nanomaterials*. 2025; 8(2): 11330.
<https://doi.org/10.24294/can11330>

ARTICLE INFO

Received: 14 January 2025

Accepted: 20 March 2025

Available online: 19 May 2025

COPYRIGHT



Copyright © 2025 by author(s).

Characterization and Application of Nanomaterials is published by EnPress Publisher, LLC. This work is licensed under the Creative Commons Attribution (CC BY) license.

<https://creativecommons.org/licenses/by/4.0/>

Abstract: This study examined the impact of aluminium doping on the structural, electrical, and magnetic properties of $\text{Li}_{(0.5)}\text{Co}_{(0.75)}\text{Al}_x\text{Fe}_{(2-x)}\text{O}_4$ spinel ferrites ($x = 0.15$ to 0.60). The samples were synthesised using the sol-gel auto-combustion technique, and they were examined using X-ray diffraction (XRD), scanning electron microscopy (SEM), Fourier-transform infrared spectroscopy (FTIR), dielectric measurements, and vibrating sample magnetometry (VSM). All samples possessed a single-phase cubic spinel structure with Fd-3m space group, according to XRD analyses. SEM images showed the creation of homogeneous particles with an average size of about 21 nm. All samples had spinel ferrite phases, confirmed from FTIR spectra. DC electrical conductivity studies showed that the conductivity increased with increasing aluminium content up to $x = 0.45$ before dropping at $x = 0.60$. The maximum saturation magnetization value was found at $x = 0.45$, according to VSM measurements, which demonstrated that the magnetic characteristics were strongly correlated with the amount of aluminium.

Keywords: ferrites; structural studies; morphology; magnetic materials

1. Introduction

Ferrites are a class of magnetic materials with a wide range of technological applications, including in microwave devices, transformers, and magnetic recording media [1]. Ferrites are typically composed of iron oxide (Fe_2O_3) and other metal oxides, such as zinc oxide (ZnO) or nickel oxide (NiO). The properties of ferrites can be tailored for specific applications by doping them with various metal ions.

Aluminium (Al)-doped lithium cobalt (Li-Co) ferrites are a class of magnetic materials that have gained increasing attention in recent years due to their potential applications in various fields such as microwave absorption [2], magnetic recording [3], and electromagnetic interference (EMI) shielding [4]. These materials are composed of a ferrimagnetic spinel structure with a general formula of $\text{LiCo}_{1-x}\text{Al}_x\text{Fe}_2\text{O}_4$, where x represents the Al doping concentration. The Al doping in Li-Co ferrites results in a significant enhancement in the magnetic properties, such as the saturation magnetization and the coercive field, as well as an improvement in the microwave absorption characteristics.

The synthesis of Al-doped Li-Co ferrites can be achieved through various

methods such as solid-state reaction [1], sol-gel[5], the co-precipitation method [6], and hydrothermal synthesis[7]. Among these methods, the solid-state reaction method is the most commonly used due to its simplicity and cost-effectiveness. In this method, the starting materials, such as LiCoO_2 , CoO , Fe_2O_3 , and Al_2O_3 , are mixed together in a desired proportion and heated at a high temperature for several hours. The final product is then cooled and ground to a fine powder. The magnetic properties of Al-doped Li-Co ferrites are strongly influenced by the Al doping concentration. The saturation magnetization increases with increasing Al doping concentration, reaching a maximum at $x = 0.1$. This is due to the substitution of Al^{3+} ions for Co^{2+} ions in the ferrite structure, which results in a decrease in the average spin state of the Co ions and a corresponding increase in the magnetic moment. The coercive field also increases with increasing Al doping concentration, which indicates an improvement in the magnetic stability of the material [8–12].

In addition to the magnetic properties, Al-doped Li-Co ferrites have been found to have excellent microwave absorption characteristics [9]. The absorption peak of these materials is found to be in the range of 2–18 GHz, making them suitable for use in the microwave frequency range. The absorption performance is also found to improve with increasing Al doping concentration, which is attributed to the enhancement of the magnetic loss caused by the substitution of Al^{3+} ions for Co^{2+} ions. The EMI shielding performance of the Al-doped Li-Co ferrites is also found to be good [13]. EMI is the unwanted interference caused by electromagnetic radiation and it is a major concern in many electronic devices. The shielding effectiveness of these materials is found to increase with increasing Al doping concentration, which is attributed to the improvement in the magnetic properties as well as the increase in the electrical conductivity caused by the substitution of Al^{3+} ions for Co^{2+} ions. Furthermore, the Al-doping in Li-Co ferrites is found to affect the microstructure of the materials. The Al-doping leads to the formation of smaller grain size and more homogeneous distribution of the grains. This can lead to an improvement in the mechanical properties of the materials [14].

The Al-doped Li-Co ferrites are a promising class of magnetic materials that have a wide range of potential applications due to their excellent magnetic and microwave properties. The Al-doped Li-Co ferrites concentration was synthesized by the auto-combustion method. The detailed structural studies were done through XRD, SEM, EDAX, and FTIR studies. Dielectrical, AC conductivity, and magnetic properties of these ferrites are also studied and controlled to optimize the properties of these materials for specific applications.

2. Experimental

2.1. Samples preparation

The sol-gel auto combustion method is a commonly used technique for synthesizing oxide materials, including spinel ferrites such as $\text{Li}_{0.5}\text{Co}_{0.75}\text{Al}_x\text{Fe}_{2-x}\text{O}_4$ ($x = 0.15, 0.30, 0.45, \text{ and } 0.60$).

Here are the steps to synthesize this material using the sol-gel auto combustion method:

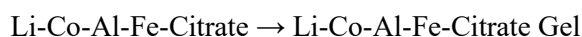
2.2. Preparation of precursor sol

The first step in the process is the preparation of a precursor sol, which is a stable colloidal suspension of nanoparticles in a liquid medium (water). In this case, the precursor compounds used are LiNO_3 , $\text{Co}(\text{NO}_3)_2 \cdot 6\text{H}_2\text{O}$, $\text{Al}(\text{NO}_3)_3 \cdot 9\text{H}_2\text{O}$, $\text{Fe}(\text{NO}_3)_3 \cdot 9\text{H}_2\text{O}$, and $\text{C}_6\text{H}_8\text{O}_7 \cdot \text{H}_2\text{O}$ from SD Fine-Chem Ltd (India). These compounds are dissolved in a suitable solvent (water) used to prepare the sol. A stabilizing agent, such as citric acid, is also added to prevent the agglomeration of nanoparticles.



2.3. Gelation

The sol is then subjected to a gelation process, which transforms the liquid sol into a solid gel matrix. Gelation can be achieved by several methods, including evaporation, cooling, or chemical crosslinking. In this case, the gelation is achieved by heating the sol at a temperature of around 80°C for several hours until a solid gel is obtained.



2.4. Auto-combustion

The solid gel matrix was initially heated at 120°C to remove excess water, followed by auto-combustion at approximately 250°C , and final sintering at 800°C for 4 h. The solid gel matrix is then heated to a high temperature to trigger the auto-combustion process. This process involves an exothermic chemical reaction between the precursor compounds and the stabilizing agent, which generates heat and produces the desired oxide products. In the first step, $\text{C}_6\text{H}_8\text{O}_7 \cdot \text{H}_2\text{O}$ (citric acid) acts as a fuel and reacts with LiNO_3 to produce $\text{Li}_5\text{C}_6\text{H}_3\text{O}_7$ (lithium citrate), NO_2 , and H_2O . The lithium citrate then reacts with the metal nitrates to form the desired oxide products, along with CO_2 , H_2O and NO_2 . The exact stoichiometry and properties of the final product depend on the composition and combustion conditions used in the process.

2.5. Final product formation



The heat generated during the auto-combustion process at ambient air causes the solid products to crystallize and form $\text{Li}_{0.5}\text{Co}_{0.75}\text{Al}_x\text{Fe}_{2-x}\text{O}_4$ ($x = 0.15, 0.30, 0.45, \text{ and } 0.60$).

3. Results and discussion

3.1. Powder XRD analysis

X-ray diffraction (XRD) of samples done by Rigaku Smartlab SE (fully automated computerized powder XRD); X-ray tube: CuAngular range (2θ): 2° to 80° with Cu-K_α radiation ($\lambda = 1.5406 \text{ \AA}$). The powder specimen of the crystal can be thought of as a group of microscopic crystals that are randomly oriented and present a range of glancing angles to the incident beam. There can only be one value of the

glancing angle that fulfils the equation $2d\sin\theta = n\lambda$, where $n = 1$, for a given wavelength and a given value of d . Such reflected beams, which are slanted at an angle of 2θ with the direction of the incident beam, radiate out from the specimen in all directions.

$$d = \frac{a}{\sqrt{h^2 + k^2 + l^2}} \text{ \AA}.$$

where, a = lattice constant, (hkl) = Miller indices.

The lattice constant is calculated by the relation [14,15],

$$a = \frac{\lambda}{2\sin\theta} \sqrt{h^2 + k^2 + l^2}$$

where, λ = wavelength of monochromatic X-rays, θ = glancing angle.

Knowing the values of (hkl) , the lattice constant may be computed for the prominent line in the spinel diffraction pattern, which corresponds to the (311) plane. We may determine the interplanar spacing by obtaining the values of the Miller indices and lattice constant.

$$d = \frac{\lambda}{2\sin\theta} \text{ or } d = \frac{a}{\sqrt{h^2 + k^2 + l^2}}$$

where, λ = wavelength of Cu- α (1.5406 \AA), θ = glancing angle.

The average particle size of each sample is calculated from the relation [16].

$$D = \frac{0.9\lambda}{\beta\cos\theta}.$$

β = full width half maximum corresponding to the highest peak of the (311) plane.

Similarly, dislocation density(ρ), lattice strain(ε), and porosity(P) are calculated from the following relations [17].

$$\rho = \frac{1}{D^2}, \varepsilon = \frac{\beta\cos\theta}{4}, P = \frac{dx-da}{dx} \times 100,$$

$$dx = X - \text{ray density} = \frac{ZM}{Na^3}.$$

Hopping lengths (L_A and L_B),

$$\text{Tetrahedral location for } A, L_A = \frac{\sqrt{3}}{4} a \text{ \AA}.$$

$$\text{Octahedron location for } B, L_B = \frac{\sqrt{2}}{4} a \text{ \AA}.$$

where Z is the number of molecules per cell, N is Avogadro's number (6.02×10^{23}), a is the lattice constant, and da is the actual density, which is equal to the mass divided by the volume of the pellet in grams.

The X-ray diffraction (XRD) patterns of the $\text{Li}_{(0.5)}\text{Co}_{(0.75)}\text{Al}_x\text{Fe}_{(2-x)}\text{O}_4$ spinel ferrites are presented in **Figure 1**. All samples exhibit a face-centered cubic (FCC) spinel structure, with no detectable secondary phases, confirming the formation of a single-phase material. The absence of any impurity peaks further supports the phase purity of the synthesized ferrites. Among the diffraction peaks, the (311) plane is observed to have the highest intensity, which is characteristic of spinel ferrites and consistent with previously reported data. The indexed diffraction peaks correspond to the (111), (220), (311), (222), (400), (422), (511), and (440) planes, aligning well with standard spinel ferrite patterns and reinforcing the structural integrity of the material.

The lattice parameters, calculated using Bragg's law, exhibit a close correlation with the experimentally observed interplanar spacings, as summarized in **Table 1**. This agreement validates the precision of the structural analysis and confirms the successful incorporation of Al^{3+} into the spinel lattice.

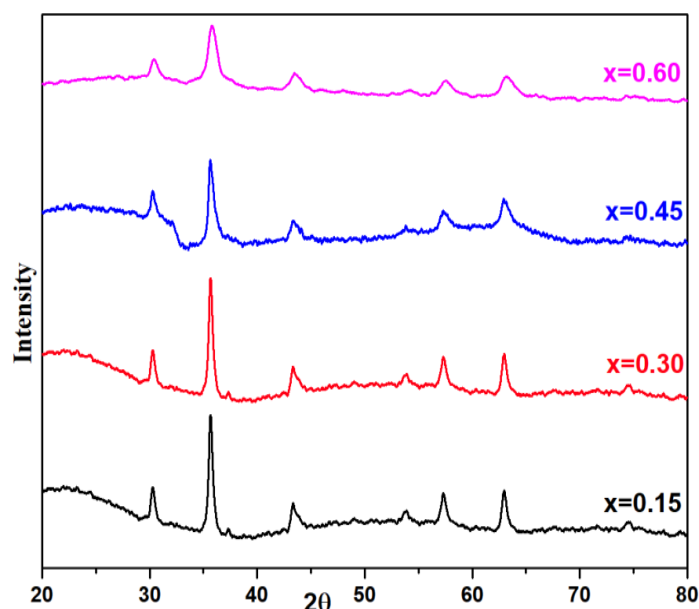


Figure 1. XRD patterns of $\text{Li}_{0.5}\text{Co}_{0.75}\text{Al}_x\text{Fe}_{2-x}\text{O}_4$ ($x = 0.15, 0.30, 0.45, \text{ and } 0.60$).

The variation of lattice parameter with composition is shown in **Table 1**. From the table it is observed that the lattice constant (a) decreases with an increase in composition. Which is attributed to the fact that as composition Al increases, the amount of Fe decreases. Because the ionic radius of Al^{3+} (0.53 Å) is less than that of Fe^{3+} (0.77 Å), hence the lattice constant tends to decrease with composition, obeying Vegard's law.

The observed deviation in lattice parameter is due to the rearrangement of Al and Fe ions. The variation of crystallite size with composition is depicted in **Table 1**. From the table, it is observed that the crystallite size nearly varies from 9 nm to 28 nm. The size is found to decrease with an increase in the composition of Al. The porosity varies from 23% to 48% depending upon the method of preparation, purity of samples, and sintering temperature (**Table 1**). It is due to the fact that X-ray density is greater than that of actual density because of the presence of pores in the material, depending on the method of preparation and sintering condition.

Table 1. Data on lattice constant, average particle size, dislocation density, lattice strain, and X-ray density.

Composition, x	Lattice constant, Å	Avg. particle size, D in nm	Dislocation density, ρ in $\times 10^{16}\text{m}^{-2}$	Lattice strain, $\varepsilon \times 10^{-3}$	X-ray density, d_x (g/cc)	Hopping length	
						L_A Å	L_B Å
0.15	8.3462	29	0.121	1.218	5.004	3.613	2.950
0.30	8.3408	20	0.283	1.845	4.912	3.611	2.948
0.45	8.3528	15	0.437	2.293	4.781	3.616	2.952
0.60	8.3663	9	1.274	3.913	4.752	3.600	2.939

3.2. FTIR analysis

Figure 2 presents FTIR spectra. The vibration mode of the space group $Fd_{3m}O_7^7$ exhibits four IR active fundamentals in the spinel ferrites with FCC structure. The largest restoring force is associated with the inherent vibrations of tetrahedral complexes, whereas bond-bending vibrations are associated with octahedral complexes. Hence, it is anticipated that $\nu_1 > \nu_2$. **Table 2** displays two distinct lines in the ranges of 572 cm^{-1} to 539 cm^{-1} and 496 cm^{-1} to 455 cm^{-1} , respectively. $\text{Fe}^{3+}-\text{O}^{2-}$ distance changes in the octahedral and tetrahedral complexes may be the cause of the minor shift in frequency with composition. Due to the presence of Fe^{2+} , which locally causes lattice deformation because of a non-cubic component of the crystal field potential, the Jahn-Teller effect splits the bands ν_1 and ν_2 . In contrast, Fe^{3+} ions don't have these effects [18,19].

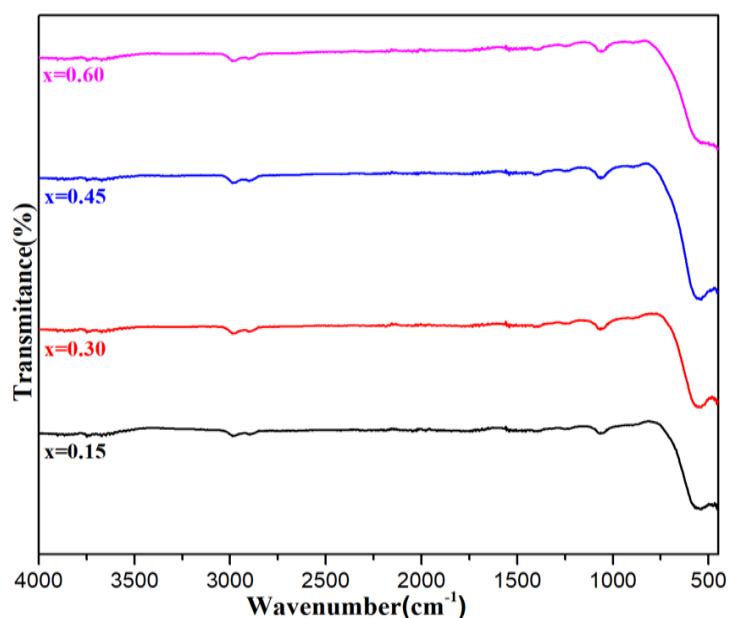


Figure 2. FTIR spectra of $\text{Li}_{0.5}\text{Co}_{0.75}\text{Al}_x\text{Fe}_{2-x}\text{O}_4$.

Table 2. Data on FTIR absorption bands of $\text{Li}_{0.5}\text{Co}_{0.75}\text{Al}_x\text{Fe}_{2-x}\text{O}_4$ ferrites.

Composition, x	Absorption bands	
	ν_1 (cm^{-1})	ν_2 (cm^{-1})
0.15	539	455
0.30	555	457
0.45	539	455
0.60	535	455

3.3. Scanning electron microscope analysis

The samples' SEM (Jeol JSM/JSM-IT500LA, magnification up to $300,000\times$ Resolution: 3nm Acc. Voltage up to 30kV Max. specimen size: 200mm Dia \times 75mm height (fully computer-controlled carbon, gold coating) micrographs are shown in **Figure 3**. The features shown in these micrographs are as follows. The sample's porosity ranges from 23% to 48% since the sol-gel process was used to

prepare them. The size of the grain varies between 17 and 26 μm depending on the heat treatment. If $x=0.15$, the largest grain size is discovered. At the base of the neck and the neck, porosity forms as a result of uneven diffusion rates. The characteristic microstructure of ferrites, in which residual porosity manifests in intra granular space, is the outcome of the mechanism of pore expansion in conjunction with grain growth. **Table 3** shows that average grain diameter reduces as aluminium content rises. The presence of a particular number of metal ion vacancies brought on by the oxidation of a suitable dopant is what causes the diameter to expand [20,21].

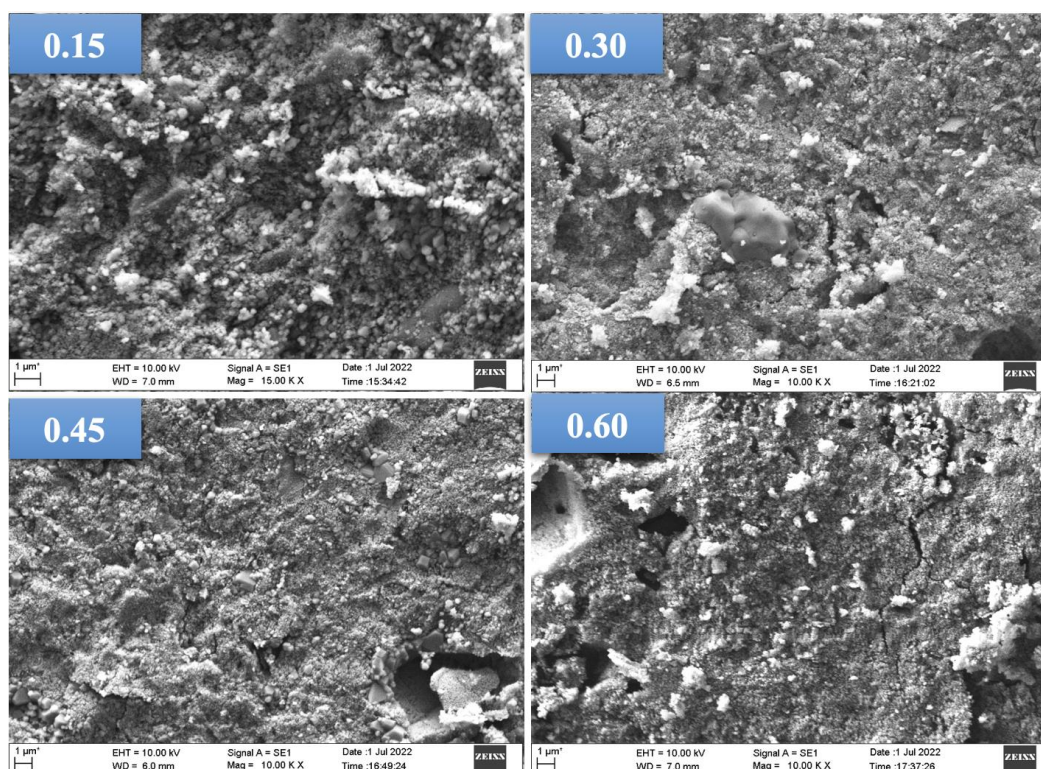


Figure 3. SEM spectrum of the $\text{Li}_{0.5}\text{Co}_{0.75}\text{Al}_x\text{Fe}_{2-x}\text{O}_4$.

Table 3. Data on actual density, porosity, and grain size.

Composition 'x'	Actual density g/cc	Porosity 'P' %	Average grain diameter 'D' in μm
0.15	3.136	23.10	25.9
0.30	3.179	39.73	22.70
0.45	3.042	36.37	20.22
0.60	2.452	48.42	17.48

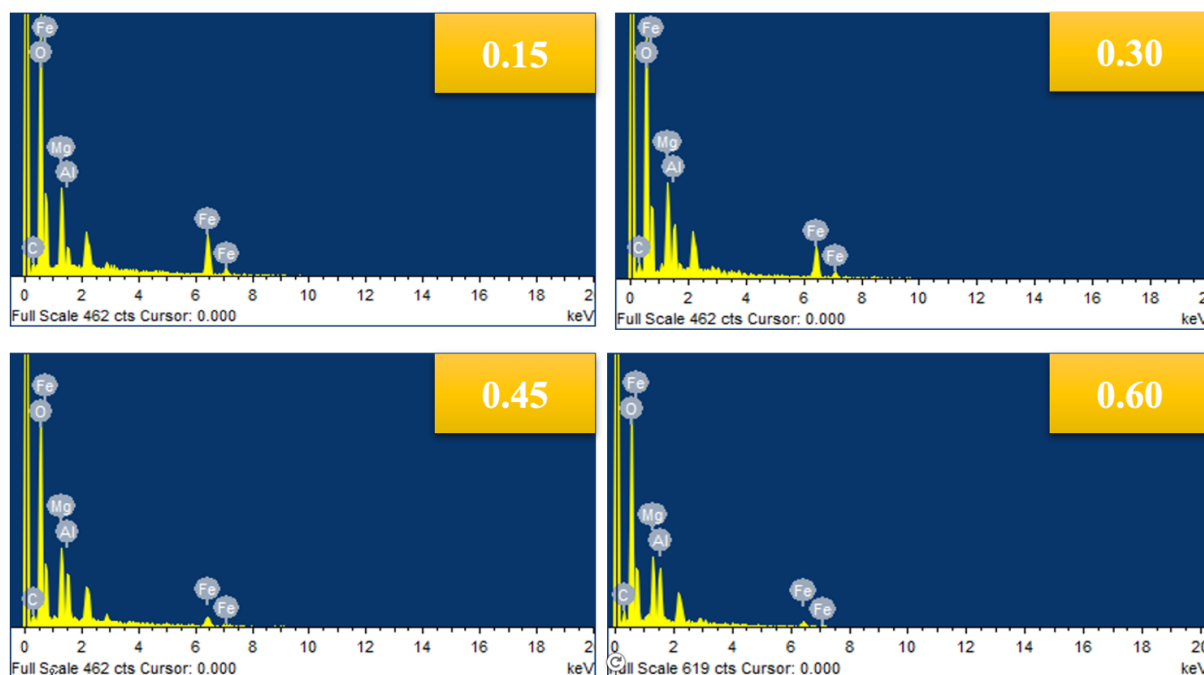


Figure 4. EDS analysis of the $\text{Li}_{0.5}\text{Co}_{0.75}\text{Al}_x\text{Fe}_{2-x}\text{O}_4$.

The elemental composition of the synthesized ferrites was confirmed using Energy Dispersive X-ray Spectroscopy (EDS). The EDX sample peaks are shown in **Figure 4**, revealing that the FCC structure is formed without any impurity. The identified elements from the EDX are Co, Al, Fe, and O, in which lithium (Li) is absent. Lithium is a light element with a low atomic number and is typically not detected using EDS due to its weak X-ray emission and other elements detected listed in **Table 4**.

Table 4. The percentage of trace elements present in the ferrite.

x	0.15		0.30		0.45		0.60	
Elements	Weight%	Atomic%	Weight%	Atomic%	Weight%	Atomic%	Weight%	Atomic%
C K	3.53	7.90	3.97	8.73	2.97	6.50	4.64	10.03
O K	33.01	55.42	32.62	53.77	33.67	55.37	33.14	53.77
Mg K	8.26	9.13	8.76	9.51	9.03	9.77	7.33	7.82
AL K	1.95	1.94	4.33	4.23	5.49	5.35	5.77	5.55
Fe L	53.24	25.61	50.32	23.76	48.84	23.01	49.13	22.83

3.4. Dielectric properties analysis

The sample in pellet form is used to measure capacitance (C_p) and dielectric loss (ϵ) at room temperature in the frequency range from 20Hz to 1MHz by the two-probe method (HIOKI-IM3570 high-precision impedance analyzer interfaced to a computer in the frequency range from 4 Hz to 1 MHz).

The dielectric constant is calculated by the relation [22].

$$\epsilon = \frac{C_p t}{\epsilon_0 A}$$

where, C_p —capacitance of the parallel plate capacitor in Farad, t —thickness of the pellet in meter, ϵ_0 —permittivity of free space in SI unit, A —area of cross section of

pellet in m^2 .

The AC conductivity is related to dielectric relaxation, caused by localized electric charges. The frequency-dependent AC conductivity is calculated from the relation:

$$\sigma_{AC} = 2\pi f \epsilon_0 \epsilon.$$

where, f = frequency of applied electric field in Hz, ϵ_0 —permittivity of free space in SI unit, ϵ —dielectric constant.

All the samples exhibit dispersion (**Figure 5a,b**) in dielectric constant in the frequency range of 20 Hz to 1 MHz. Beyond this range, it does not remain constant; it may be constant above 5 MHz. The dispersion in dielectric constant obeys Maxwell-Wagner type interfacial polarization, in agreement with Koop's phenomenological theory. The large values of the parameter at low frequency are due to space charge polarization at grain boundaries, interfacial dislocation, oxygen vacancies, grain defects and predominance of large Fe^{3+} ions [23] and abstraction belonging to the polarization due to changes in valence states of cations and space charge polarization. At higher frequencies the dielectric constant remains independent of frequency (f) due to the lack of ability of electric dipoles to follow the fast variation of the alternating applied electric field [24]. When grain size decreases, grain boundary area and porosity decrease, but in this case, porosity increases due to many effects like method of preparation, sintering condition, etc. This substitution of lithium affects grain growth, typically leading to a reduction in particle size, which in turn influences dielectric behavior. Smaller particles increase grain boundary resistance, thereby enhancing dielectric constant and loss at lower frequencies. The decrease in the parameter with frequency is due to lagging of polarizability behind the applied field at higher and higher frequency. Due to impurities and flaws in the crystal lattice, polarization sometimes lags behind the applied AC field, which results in dielectric loss [17,22–24]. The period of rest, which is comparable to the applied field duration, is what causes the most loss. The dielectric becomes tiny if the relaxation time is longer than the applied field period, and vice versa. The AC conductivity of Li-Co ferrites generally increases with increasing frequency, exhibiting semiconducting behavior due to hopping mechanisms of charge carriers, especially electrons between Fe^{2+} and Fe^{3+} ions shown in **Figure 5c**.

The conduction mechanism in ferrites is due to electrons and polarons following the hopping model suggested by Austin and Moot. The inverse tangential increase in conductivity with frequency is attributed to small polarons. Such behavior is found in all the ferrite samples. The variation in hopping length is the distance between ions in A and B sites, which governs the conduction mechanism as shown in **Table 5**. The same reports have been reported in the case of Li-Ni-Cu nano ferrites [17].

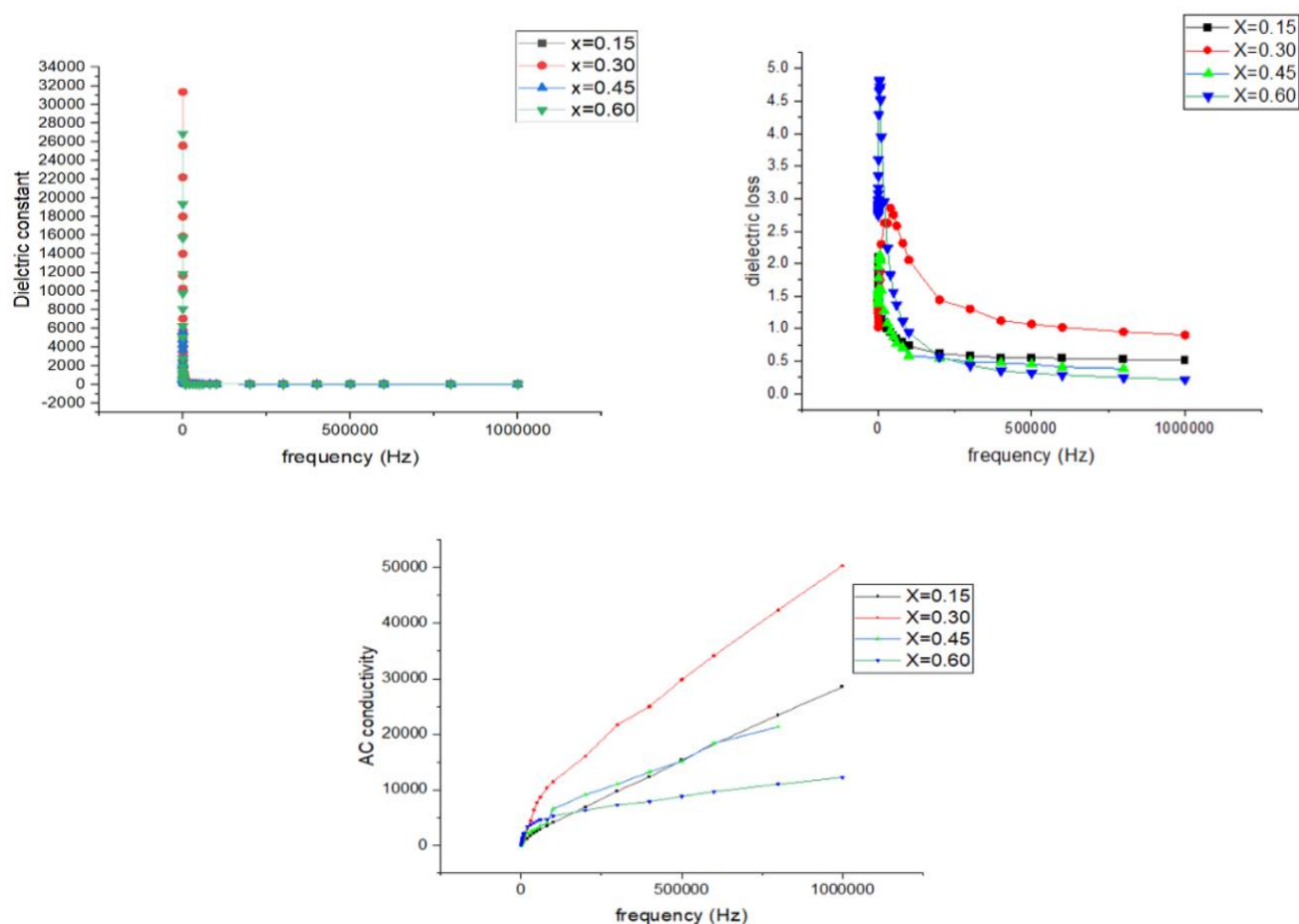


Figure 5. Dielectric studies of $\text{Li}_{0.5}\text{Co}_{0.75}\text{Al}_x\text{Fe}_{2-x}\text{O}_4$ nano ferrites (a) dielectric constant; (b) dielectric loss factor; (c) AC conductivity.

Table 5. Data on porosity, hopping length, and AC conductivity at 1 MHz.

Composition, x	Lattice constant, a Å	Porosity, P %	AC conductivity, $\sigma \text{ Sm}^{-1}$
0.15	8.3482	23.10	28,513.712
0.30	8.3408	39.73	50,295.760
0.45	8.3528	36.37	21,300.360
0.60	8.3163	48.42	12,199.196

3.5. Magnetic properties analysis

The specification of the VSM analyzer: Lakeshore, model: 7410 series. The variation of saturation magnetization vs. alternating magnetizing field of all the samples at room temperature (300 K) is shown in **Figure 6**. The data on saturation magnetization, magnetic moment, and H_c are given in **Table 6**.

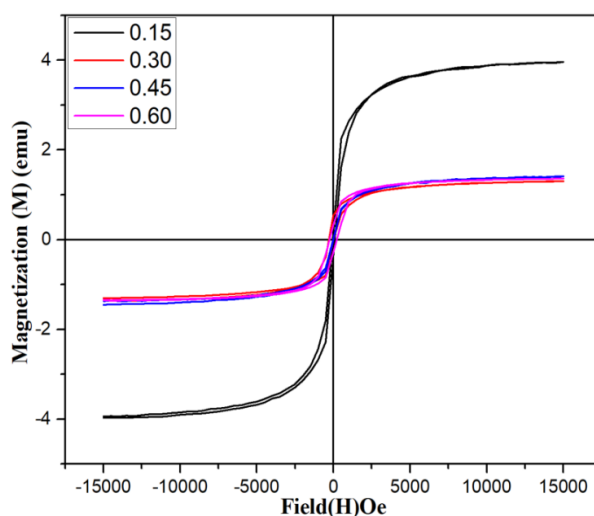


Figure 6. Magnetic properties study of $\text{Li}_{0.5}\text{Co}_{0.75}\text{Al}_x\text{Fe}_{2-x}\text{O}_4$ nano ferrites.

Table 6. Different magnetic parameters for all Al-substituted Li-Co ferrites.

Composition, x	Molecular weight, M	Saturation magnetization, M_s	μ_B	Coercivity (H_c) (Oe)	Porosity
0.15	219.02	3.97	0.1556	512	37.36
0.30	214.69	1.33	0.0511	498	46.06
0.45	210.36	1.43	0.0538	473	36.37
0.60	206.03	1.36	0.0501	447	52.71

The variation of magnetic moment with Al can be explained as follows. Both Al and Li are nonmagnetic in nature. As the amount of Al increases, the amount of Fe^{3+} ions on both A and B sites decreases. As a result, magnetization goes on decreasing with an increase in Al. However, the variation of M_s with composition is attributed to the density of the sample. This then results in the weakening of A–B exchange interactions and decreases the saturation magnetization. At $x = 0.15$, it exhibits the highest saturation magnetization (~ 4 emu) due to the strong $\text{Fe}^{3+}\text{--O}^{2-}\text{--Fe}^{3+}$ super exchange interactions. As Al^{3+} substitution increases ($x = 0.30$ to 0.60), the magnetization decreases because non-magnetic Al^{3+} ions replace Fe^{3+} , weakening the overall magnetic interactions. This substitution disrupts the spin alignment, leading to a decline in the net magnetic moment. This then results in the weakening of A–B exchange interactions and increases the saturation magnetization [25–27]. Due to polarization effects, they prefer tetrahedral and octahedral sites, and the presence of non-magnetic lithium-aluminium ions in these sites results in lower values than both sites and consequently enhancement of M_s values [27–29]. Similarly, the coercivity is highest for $x = 0.15$, indicating hard magnetic behavior. As Al^{3+} content increases, it decreases, suggesting a transition to a softer magnetic nature. This reduction in coercivity results from the dilution of magnetic interactions and a decrease in anisotropy, making the material easier to magnetize and demagnetize. The observed changes confirm that Al^{3+} substitution significantly influences the structural and magnetic properties of $\text{Li}_{(0.5)}\text{Co}_{(0.75)}\text{Al}_x\text{Fe}_{(2-x)}\text{O}_4$ spinel ferrites. Microstructure is a significant additional aspect that affects ferrites' ability to magnetize. Every grain possesses a unique magnetic moment. The magnetic circuits between the grains are

broken by the pores. As a result, there are net reductions in magnetic moment and an increase in porosity. Smaller numbers of big grains are formed at higher a sintering temperature, which reduces porosity. Hence, magnetism rises as sintering temperature rises [26–29].

4. Conclusion

In conclusion, the study investigated the effects of aluminium doping on the structural, electrical, and magnetic properties of $\text{Li}_{(0.5)}\text{Co}_{(0.75)}\text{Al}_x\text{Fe}_{(2-x)}\text{O}_4$ spinel ferrites ($x = 0.15$ to 0.60) synthesized using the sol-gel auto-combustion technique. The results showed that the samples had a single-phase cubic spinel structure with Fd-3m space group, confirmed by XRD analysis. SEM images showed the creation of homogeneous particles with an average size of about 21 nm. FTIR spectra confirmed the presence of spinel ferrite phases in all samples. The DC electrical conductivity increased with increasing aluminium content up to $x = 0.45$ before dropping at $x = 0.60$. The maximum saturation magnetization value was found at $x = 0.45$, indicating a strong correlation between the magnetic properties and the amount of aluminium. Therefore, the study suggests that the addition of aluminium can significantly enhance the magnetic and electrical properties of $\text{Li}_{(0.5)}\text{Co}_{(0.75)}\text{Fe}_{(2)}\text{O}_4$ spinel ferrites, up to a certain point, which can be beneficial for various technological applications.

Author contributions: Conceptualization, KPM and MGK; methodology, SVA; software, KPM and MGK; validation, LDH, SNM, SSK, CSH, MSB and RBP; formal analysis, RBP, SSK and SNM; investigation, KPM and MGK; resources, KPM, MGK and RBP; data curation, KPM and MGK; writing—original draft preparation, KPM, MGK and SSK; writing—review and editing, SNM and RBP; supervision, SNM and RBP; project administration, CSH, LDH and RBP. All authors have read and agreed to the published version of the manuscript.

Institutional review board statement: Not applicable.

Informed consent statement: Not applicable.

Conflict of interest: The authors declare no conflict of interest.

References

1. Kakati S, Rendale MK, Mathad SN. Synthesis, Characterization, and Applications of CoFe_2O_4 and $\text{M-CoFe}_2\text{O}_4$ ($\text{M} = \text{Ni}, \text{Zn}, \text{Mg}, \text{Cd}, \text{Cu}, \text{RE}$) Ferrites: A Review. *International Journal of Self-Propagating High-Temperature Synthesis*. 2021; 30(4): 189-219. doi: 10.3103/s1061386221040038
2. Choi W, Mallesh S, Ko H, et al. Fabrication of thin and lightweight cobalt-coated quartz fiber/aluminosilicate composites for high-temperature microwave absorption. *Ceramics International*. 2023; 49(9): 13586-13600. doi: 10.1016/j.ceramint.2022.12.235
3. Venkatachalapathy R, Manoharan C, Venkateshwarlu M, et al. Solution combustion route for Ni and Al co-doped lithium ferrite nanoparticles: Synthesis, the effect of doping on the structural, morphological, optical, and magnetic properties. *Ceramics International*. 2023; 49(4): 6594-6607. doi: 10.1016/j.ceramint.2022.10.212
4. Xiao C, Wang B, Zhao D, et al. Comprehensive investigation on Lithium batteries for electric and hybrid-electric unmanned aerial vehicle applications. *Thermal Science and Engineering Progress*. 2023; 38: 101677. doi: 10.1016/j.tsep.2023.101677
5. Kakati S.S, Makandar T.M, Rendale M.K, et al. Green Synthesis Approach for Nanosized Cobalt Doped Mg–Zn through Citrus Lemon Mediated Sol–Gel Auto Combustion Method. *International Journal of Self-Propagating High-Temperature*

- Synthesis. 2022; 31(3): 131-137. doi: 10.3103/s1061386222030049
6. Kashid P, Shedam M, Kulkarni AB, et al. Synthesis and Structural Studies of Nano $\text{Co}_{0.85}\text{Cd}_{0.15}\text{Fe}_2\text{O}_4$ Ferrite by Co-Precipitation Method. *Journal of Advanced Physics*. 2017; 6(4): 545-548. doi: 10.1166/jap.2017.1373
 7. Hu S, Wang C, Zhou L, et al. Hydrothermal-assisted synthesis of surface aluminum-doped LiCoO_2 nanobricks for high-rate lithium-ion batteries. *Ceramics International*. 2018; 44(13): 14995-15000. doi: 10.1016/j.ceramint.2018.05.128
 8. Zhang W, Gan J, Li L, et al. Tailoring of optical and electrical properties of transparent and conductive Al-doped ZnO films by adjustment of Al concentration. *Materials Science in Semiconductor Processing*. 2018; 74: 147-153. doi: 10.1016/j.mssp.2017.10.028
 9. Bu IYY. Sol-gel production of Cu/Al co-doped zinc oxide: Effect of Al co-doping concentration on its structure and optoelectronic properties. *Superlattices and Microstructures*. 2014; 76: 115-124. doi: 10.1016/j.spmi.2014.09.011
 10. Tseng YT, Choudhury A, Peng KC, et al. Concentration effect of aluminum nitrate on the Crystalline-Amorphous transition between Al-doped ZnO nanorods and nanostructures prepared by electrochemical deposition. *Electrochimica Acta*. 2019; 308: 350-362. doi: 10.1016/j.electacta.2019.04.006
 11. Kalyani CH, Subba Reddy IV, Raju P, et al. Effects of Al^{3+} concentration on the structural, dielectric and conductivity properties of Al-doped ZnO. *Materials Today: Proceedings*. 2023; 80: 1111-1115. doi: 10.1016/j.matpr.2022.12.005
 12. Wang D, Qu Z, Wang Y, et al. Effects of Al-doping concentration on the structure and electromagnetic shielding properties of transparent Ag thin films. *Optical Materials*. 2023; 135: 113353. doi: 10.1016/j.optmat.2022.113353
 13. Srinivas C, Naga Praveen K, Ranjith Kumar E, et al. Microwave absorption properties of rare earth (RE) ions doped Mn-Ni-Zn nanoferrites (RE = Dy, Sm, Ce, Er) to shield electromagnetic interference (EMI) in X-band frequency. *Ceramics International*. 2022; 48(22): 33891-33900. doi: 10.1016/j.ceramint.2022.07.338
 14. El-Moneim AA, Mazen SA, Abu-Elsaad NI. Evaluating the theoretical elastic properties of Li-Mn ferrites: A new approach. *Materials Chemistry and Physics*. 2022; 291: 126679. doi: 10.1016/j.matchemphys.2022.126679
 15. Totagi RS, Choudhari NJ, Kakati SS, et al. Electrical properties of Ni-Mg-Cu nanoferrites synthesized by sucrose precursor technique. *Scholars Research Library Der Pharma Chemica*. 2015; 7(3): 11-15.
 16. Shidaganal LC, Gandhad SS, Hiremath CS, et al. Effect of Al doping on structural and mechanical properties of Ni-Cd ferrites. *AIP Conference Proceedings*. 2018; 1953: 130025. doi: 10.1063/1.5033169
 17. Adarakatti SN, Pattar VS, Korishettar PK, et al. Synthesis, Structural and Electrical Studies of Li-Ni-Cu Nano Ferrites. *Acta Chemica Iasi*. 2018; 26(1): 1-12. doi: 10.2478/achi-2018-0001
 18. Pujar AS, Kulkarni AB, Mathad SN, et al. Structural, Electrical, and IR Properties of $\text{Cu}_x\text{Co}_{1-x}\text{Fe}_2\text{O}_4$ ($x = 0, 0.4, 1.0$) Prepared by Solid-State Method. *International Journal of Self-Propagating High-Temperature Synthesis*. 2018; 27: 174-179.
 19. Patil MR, Rendale MK, Mathad SN, et al. FTIR spectra and elastic properties of Cd-substituted Ni-Zn ferrites. *International Journal of Self-Propagating High-Temperature Synthesis*. 2017; 26(1): 33-39.
 20. Durgadsimi SU. Synthesis and structural analysis of nickel ferrite synthesized by co-precipitation method. *Eurasian Physical Technical Journal*. 2021; 18(4 (38)): 14-19. doi: 10.31489/2021no4/14-19
 21. Shashidharagowda H, Mathad S, Abbigeri M. Structural, vibrational and magnetic characterization of copper doped CoMn_2O_4 nano-particles synthesized by chemical route. *Science of Sintering*. 2021; 53(4): 429-444. doi: 10.2298/sos2104429s
 22. Yang M, Zhou W, Liu Y, et al. $\text{LiCo}_x\text{Ni}_{1-x}\text{O}_2$ with high dielectric and microwave absorption performance in X-band. *Ceramics International*. 2019; 45(14): 17800-17805. doi: 10.1016/j.ceramint.2019.05.351
 23. Goel S, Garg A, Baskey H.B, et al. Studies on dielectric and magnetic properties of barium hexaferrite and bio-waste derived activated carbon composites for X-band microwave absorption, *Journal of Alloys and Compounds*. 2021.
 24. Mathad S.N, Jadhav R.N, Pawar R.P, et al. Dielectric spectroscopy and microwave conductivity of bismuth strontium manganites at high frequencies. *Electronic Materials Letters*. 2013; 9(1): 87-93. doi: 10.1007/s13391-012-2109-8
 25. Mudholakar KP, Vinaykumar S, Tambe V.V, et al. Effect of Sintering condition on Magnetization and Microstructure of $\text{Cu}_x\text{Co}_{(1-x)}\text{Fe}_2\text{O}_4$ Ferrites. *International Journal of Advanced Science and Engineering*. 2022; 9(2): 2678-2685. doi: 10.29294/ijase.9.2.2022.2678-2685
 26. Zeeshan T, Anjum S, Waseem S, et al. Influence of zinc substitution on structural, elastic, magnetic and optical properties of cobalt chromium ferrites. *Materials Science-Poland*. 2021; 39(1): 139-151. doi: 10.2478/msp-2021-0008
 27. Jahan N, Khandaker J.I, Das H, et al. Structural and magnetic properties analysis of trivalent Al^{3+} ions substituted Ni-Zn-Co nano-spinel ferrites. *Advances in Natural Sciences: Nanoscience and Nanotechnology*. 2021; (4):045001.

28. Modi KB, Gajera J.D, Chhantbar M.C, et al. Structural properties of magnesium and aluminium co-substituted lithium ferrite. *Materials Letters*. 2003.
29. Kuru M, Kılıç Dokan F, Şaşmaz Kuru T. Structural, electrical and magnetic characterization of Al³⁺ substituted Mg–Zn ferrites. *Applied Physics A*. 2022; 128(4). doi: 10.1007/s00339-022-05443-x